

Contents

1. Analytical calculation of camera images in optical quadrature microscopy.....	3
2. Comparison of darkfield and interferometric contrast	3
3. Correction of the illumination phase.....	3
4. Refocussing.....	4
5. Angle of incidence	4
6. Measurement of the laser coherence length.....	4
Supplementary Figures.....	5
Supplementary Figure 1 – Reconstruction of holographic images.....	5
Supplementary Figure 2 – Coherence length measurement.....	6
Supplementary Figure 3 – Amplitude and phase decoupling.....	6
Supplementary Figure 4 – Phase stability with and without correction.	7
Supplementary Figure 5 – Comparison of holographic and synthetic darkfield contrast histogram.	8
Supplementary Figure 6 – Positional dependence of the phase.	9
Supplementary Figure 7 – Localisation precision.	10
Supplementary Figure 8 – Precision of the PSF fit.....	10
Supplementary Figure 9 – Single-protein contrast vs focusing during post-processing. .	11
Supplementary Figure 10 – Photograph of the optical setup.....	12
Supplementary Figure 11 – Signal-to-noise.	12
Supplementary Figure 12 – Selection criteria for protein landing events.....	13

1. Analytical calculation of camera images in optical quadrature microscopy

The idealised data shown as illustration in Fig. 1b are based on multiple scatterers with equal scattering strength but arbitrary phase and position in the image. For this, the signal of each scatterer is calculated with the complex PSF (eq. 3) and summed to one complex image. To generate the detected images for the four cameras, a phase shift $\Delta\Phi$ of 0, $\frac{\pi}{2}$, π , or $\frac{3\pi}{2}$ is applied by multiplying with $e^{i\Delta\Phi}$ before discarding the imaginary part of the image. The amplitude and phase images shown in the lower panel are obtained by taking the absolute and complex angle of the complex image, respectively. In the calculation, no noise or background is added.

2. Comparison of darkfield and interferometric contrast

In Supplementary Figure 5, a comparison between the interferometric image of single proteins measured with holography and the corresponding darkfield image of the same particles is shown. The darkfield image is obtained by squaring the complex scattering field before the calculation of the moving difference. To explain the striking difference between the two cases, it is useful to separate the scattering into a static contribution from the glass surface and the scattering by the protein. In the interferometric case, we detect

$$I_j^{cam} = |E_{ref}|^2 + |E_{scat,glass}|^2 + |E_{scat,protein}|^2 + 2|E_{ref}||E_{scat,glass}|\cos(\Delta\Phi_j) + 2|E_{ref}||E_{scat,protein}|\cos(\Delta\Phi_j) + 2|E_{scat,glass}||E_{scat,protein}|$$

assuming a scattering phase of 0 for both glass and protein. The moving difference processing eliminates constant terms and using $|E_{ref}| \gg |E_{scat,glass}| > |E_{scat,protein}|$ yields the following approximation for a landing event:

$$\Delta I_j^{cam} = |E_{scat,protein}|^2 + 2|E_{ref}||E_{scat,protein}|\cos(\Delta\Phi_j) + 2|E_{scat,glass}||E_{scat,protein}| \approx 2|E_{ref}||E_{scat,protein}|\cos(\Delta\Phi_j)$$

In the darkfield case, there is no reference field and we detect:

$$I_j^{cam} = |E_{scat,glass}|^2 + |E_{scat,protein}|^2 + 2|E_{scat,glass}||E_{scat,protein}|$$

Again, by calculating the moving difference and assuming a small protein $|E_{scat,glass}| \gg |E_{scat,protein}|$, the equation can be approximated as:

$$\Delta I_j^{cam} = |E_{scat,protein}|^2 + 2|E_{scat,glass}||E_{scat,protein}| \approx 2|E_{scat,glass}||E_{scat,protein}|$$

Unlike $|E_{ref}|$, the glass scattering $|E_{scat,glass}|$ is spatially inhomogeneous. Therefore, the darkfield image of proteins is distorted in both, shape and intensity.

3. Correction of the illumination phase

The scattering field, taking the illumination field (Fig. 4a) into account, can be described by:

$$E_{scat}(x, y) = s e^{i\varphi} E_{illu}(x, y) \approx s e^{i\varphi} |E_{illu}(x, y)| e^{i(m_x x + m_y y)}$$

Where s and φ are the intrinsic scattering amplitude and phase of the protein, $E_{illu}(x, y)$ the illumination field, and m_x and m_y the phase gradient along x and y due to the oblique angle of incidence. Inspection of the phase difference of all landing events as a function of their position along the illumination direction reveals a linear correlation (Supplementary Figure 6). We make use of this linear correlation to find a slope m_x along the illumination direction and

m_y perpendicular to it which removes the linear phase gradient. We then subtract a linear phase of each landing event phase φ_i such that $\varphi_{i,corr} = \varphi_i - (m_x x_i + m_y y_i)$

where x_i and y_i denote the landing position of the landing event i . Applying this correction ($m_x = 2.40$ rad/px, $m_y = -0.04$ rad/px) to all landing events globally (Fig. 4b, black data points) shifts the phases of almost all events onto a straight line (Fig. 4b, red data points) and minimally deviates from a constant behaviour after the linear correction due to non-perfect focussing of the illumination (Supplementary Figure 6c). The corrected phase becomes less well defined the lower the contrast of the particle. Supplementary Figure 7 suggests that the localisation precision substantially decreases with lower contrast. This affects the phase correction, which utilises the position of the landing event as confirmed by the simulation of the mass-dependent fit uncertainty presented in Supplementary Figure 8.

4. Refocussing

To refocus the complex image, a frequency-dependent phase shift is applied in Fourier-space: The phase shift is defined as

$$\Delta\varphi(k_x, k_y) = \Delta z k_z(k_x, k_y) = \Delta z \sqrt{k^2 - k_x^2 - k_y^2}$$

with k the wavevector in the medium (water) and Δz the focus offset. For frequencies above the support ($k^2 < k_x^2 + k_y^2$), the phase shift is set to 0. To apply the phase shift, the image is Fourier transformed, multiplied by $e^{i\Delta\varphi}$, and back transformed to real space.

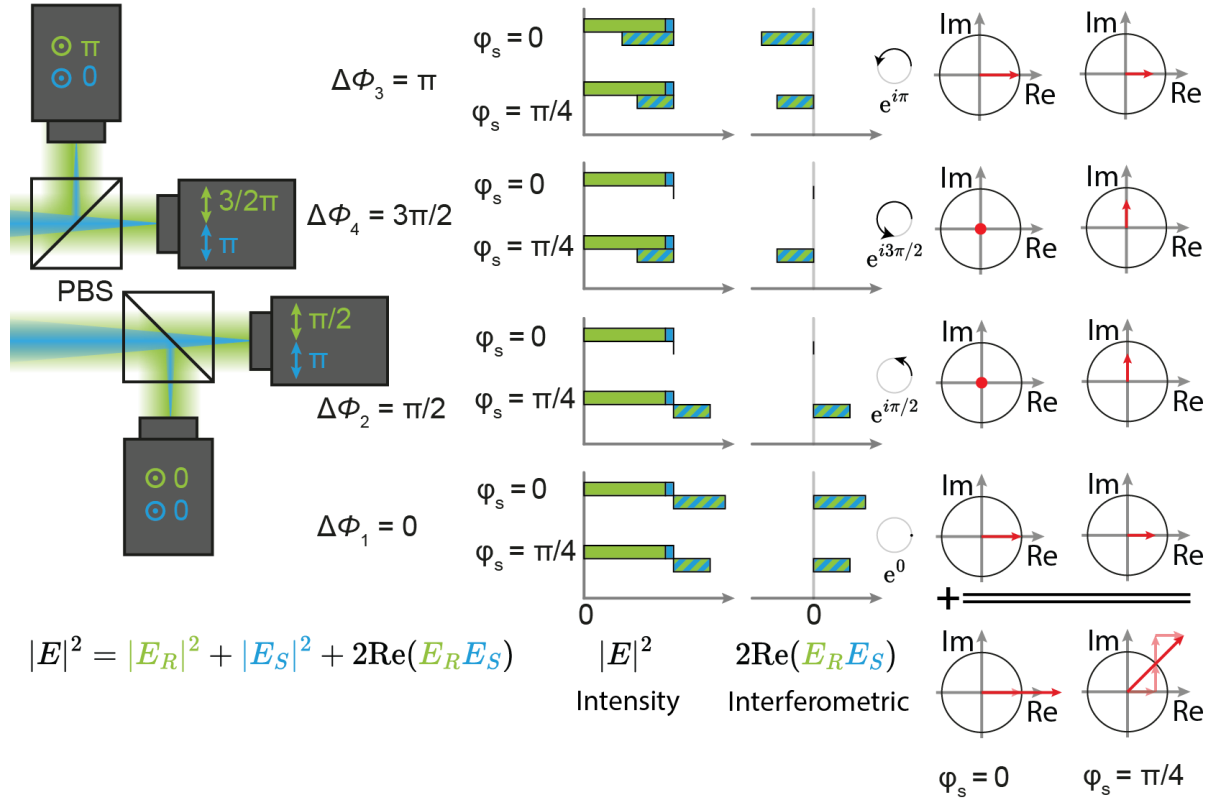
5. Angle of incidence

We used the slope of our phase correction to determine the angle of incidence. The phase correction of about 2.4 rad / px can be easily transferred into 48.83 nm / rad utilising the total magnification of 100x given by the focal lengths of the used lenses. This translates to 306.8 nm / wave at the interface. Using trigonometry, we can estimate the angle of incidence to 74.8° assuming the vacuum wavelength of 450 nm and a refractive index of $n = 1.52$ for the coverslip.

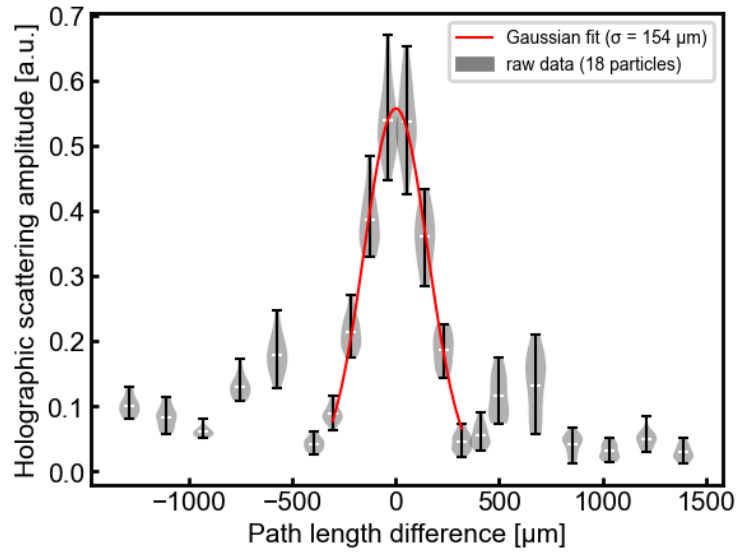
6. Measurement of the laser coherence length

To determine the coherence length of the diode laser, measurements similar to the phase-shifting measurements in Figure 2 were performed with a 60 nm AuNP sample. The path length difference was changed by translating the piezo controlled stage with an additional micrometer head. For each stage position, the average holographic scattering amplitude was measured while modulating the phase. This modulation strength was divided by the square-root of the darkfield scattering intensity to compensate differences in illumination intensity. For each position, the same field of view with 18 particles was measured. The translation of the stage was converted into a path length difference taking the angle of incidence of 19° on the translated mirror into account. A Gaussian fit of the normalised modulation strength yields a coherence length of $\sigma = 154$ μm . In the plot of the data in Supplementary Figure 2, the centre of the Gaussian fit is defined as a path length difference of zero.

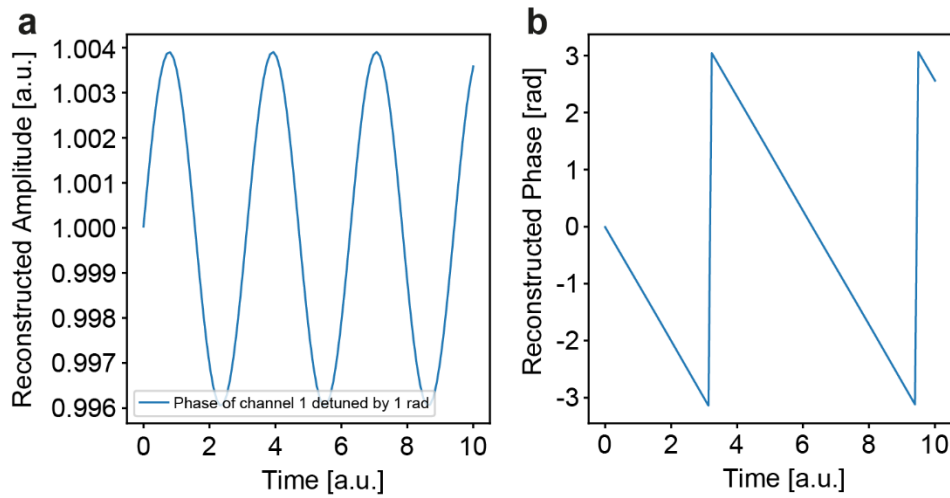
Supplementary Figures



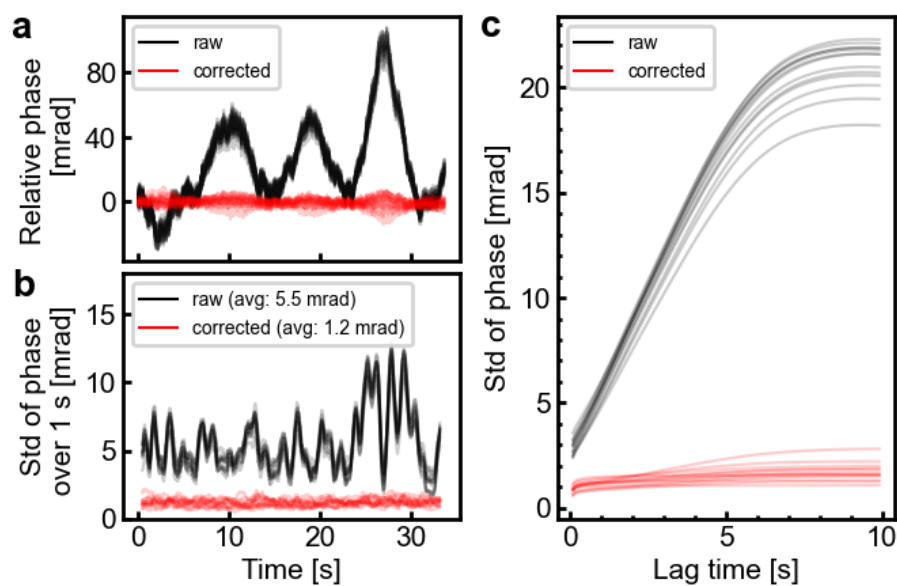
Supplementary Figure 1 – Reconstruction of holographic images. All cameras receive light with a different relative phase shift between the reference field E_R and the scattering field E_S . The interferometric component is calculated for each camera by subtracting the pre-recorded reference intensity $|E_R|^2$ and scattering intensity $|E_S|^2$. The unnormalised complex scattering field is obtained by summing all interferometric components after correcting for their respective phase shifts.



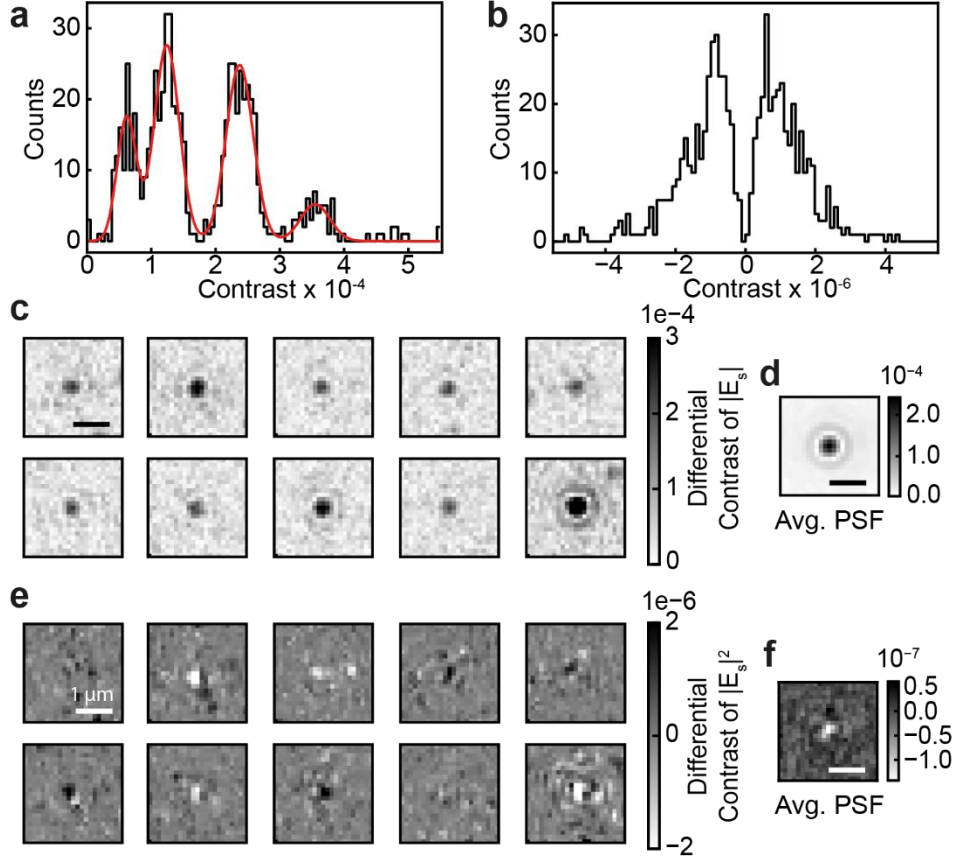
Supplementary Figure 2 – Coherence length measurement. Modulation strength as a function of the path length difference. The violins represent the distribution over 18 measured particles. The error bars show the minimum and maximum value. The Gaussian fit to the average values (white marker) indicates a coherence length of 154 μm . The measurement procedure is described in detail in supplementary section 6.



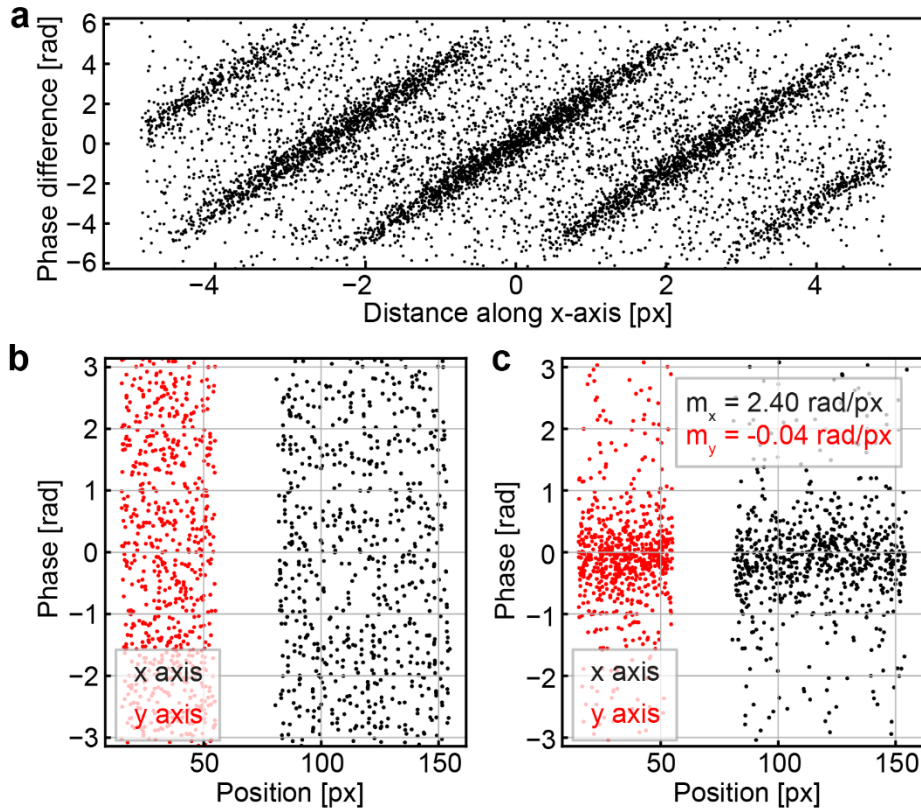
Supplementary Figure 3 – Amplitude and phase decoupling. **a** Reconstructed amplitude and **b** reconstructed phase of synthetic data while the phase of one reference arm is detuned by 0.01 rad from $\pi/2$.



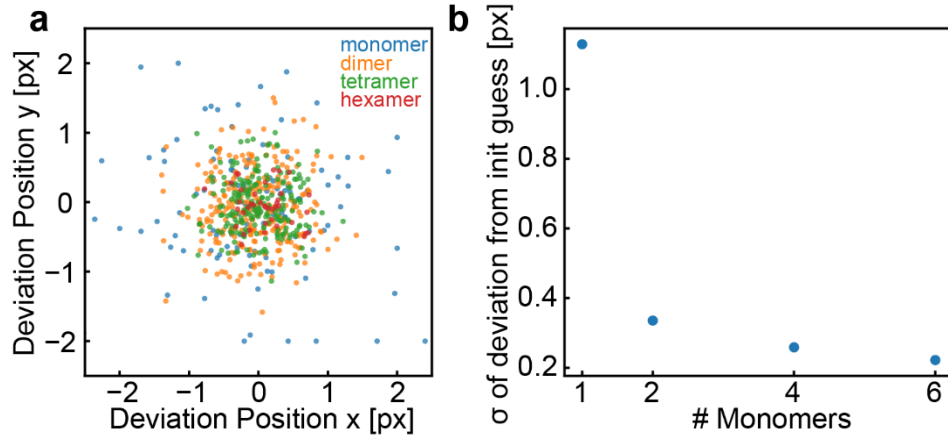
Supplementary Figure 4 – Phase stability with and without correction. **a** Phase over time for 60 nm Au NPs. The phase is set to zero for the first frame. The correction is performed as described in the method section by finding the phase that minimises the difference between the current and the first image. In all panels, the traces of 14 particles are shown. **b** Sliding standard deviation of the phase traces with a window size of 1 s. **c** Average sliding standard deviation as a function of the window size.



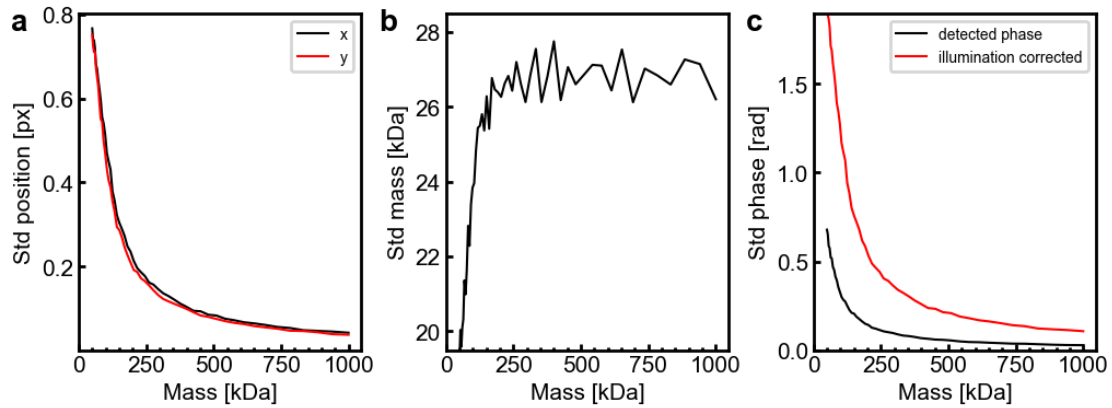
Supplementary Figure 5 – Comparison of holographic and synthetic darkfield contrast histogram. **a** Histogram of the landing event contrast determined by fitting the scattered field E_{scat} with a complex, holographic PSF of one movie. **b** Histogram of the contrast from the same landing events fitted in a synthetic darkfield movie. The darkfield movie was generated by calculating the square of the absolute of the scattering field $|E_{scat}|^2$ where E_{scat} was derived by our holographic approach. **c** Example PSFs of landing events in the holographic movie and **d** the average PSF of all fitted events. **e** Example PSFs of the same landing events in the synthetic darkfield movie and **f** the average PSF. Panels **c** and **e** show the exact same landing events.



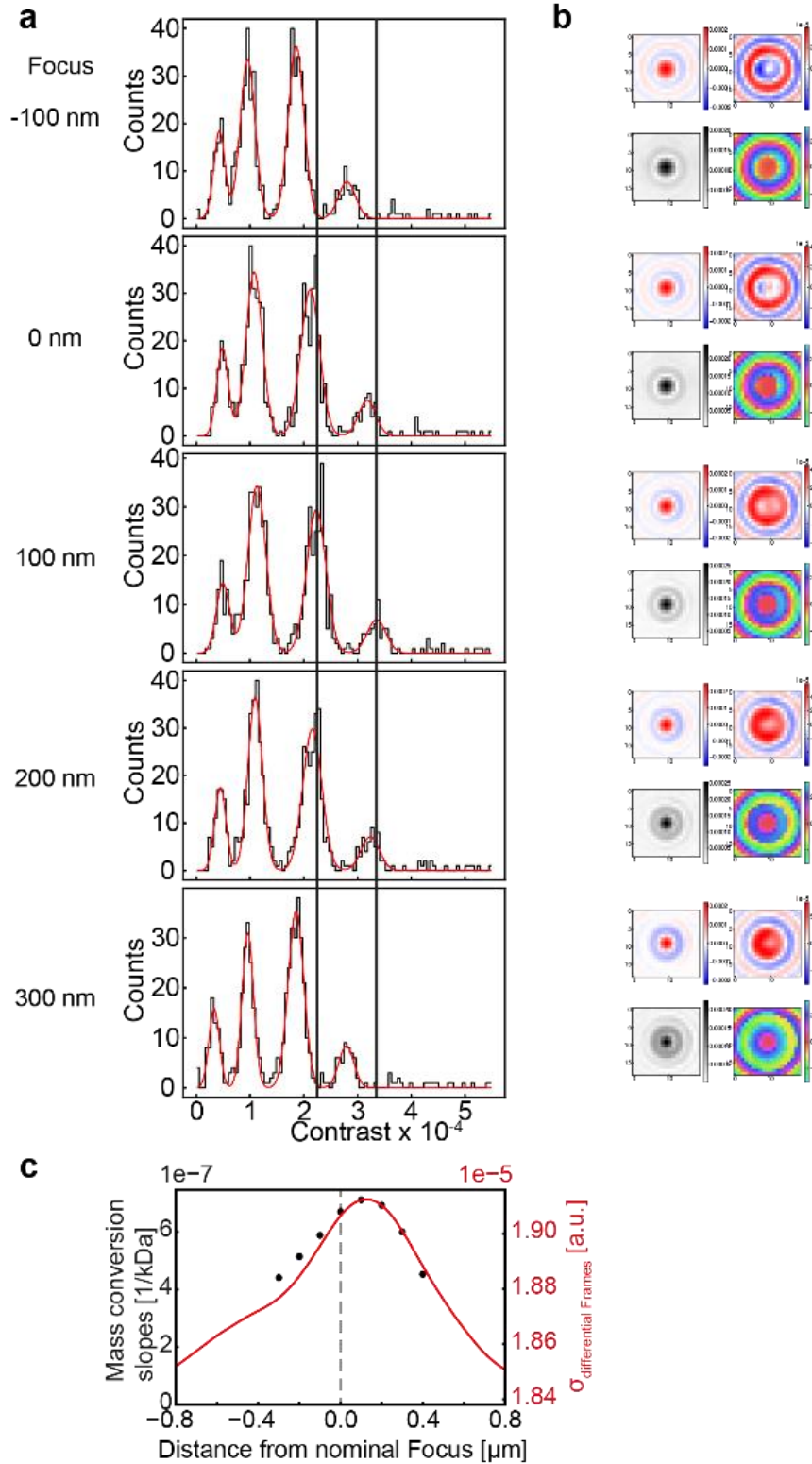
Supplementary Figure 6 – Positional dependence of the phase. **a** Difference of the detected phase $\Delta\varphi$ of individual landing particles vs their distance in landing position along the illumination direction. The linear correlation of $\Delta\varphi$ and distance relates to the oblique angle of illumination. **b** Phase of the particles before the linear phase correction. Black data points correspond to the phase along the x axis, red points represent the phase values along the y axis. **c** Phase values after subtracting a linear phase correction (black data: x axis, red data: y axis). The slopes were identified as $m_x = 2.40 \text{ rad/px}$, $m_y = -0.04 \text{ rad/px}$.



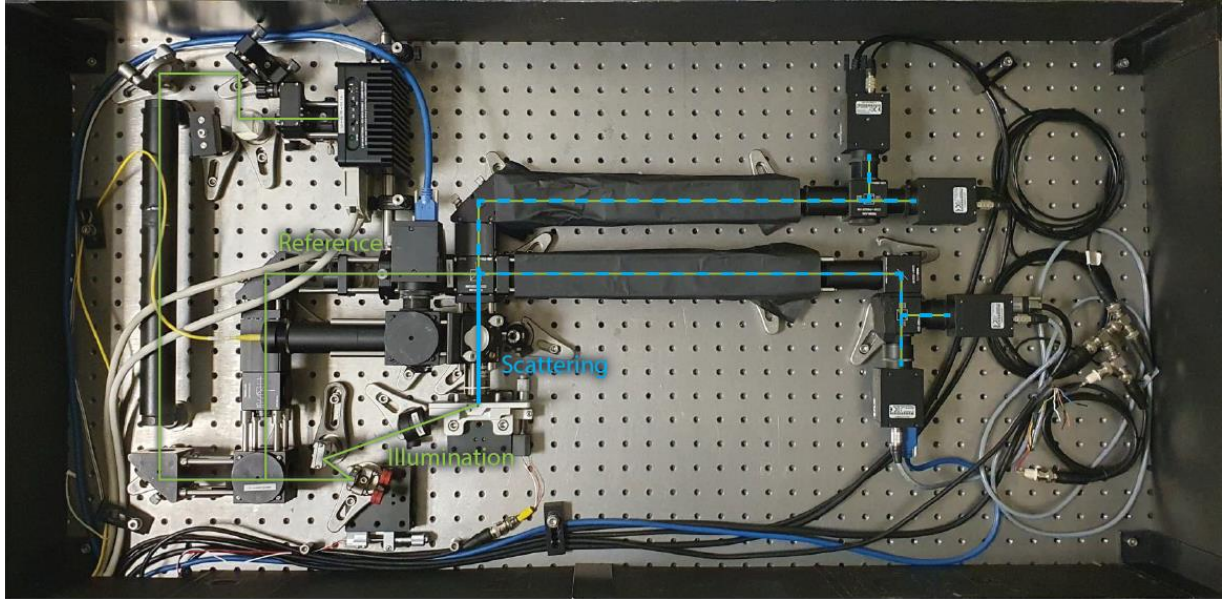
Supplementary Figure 7 – Localisation precision. **a** Deviation of fitted position from initial guess. **b** width of distributions in **a**.



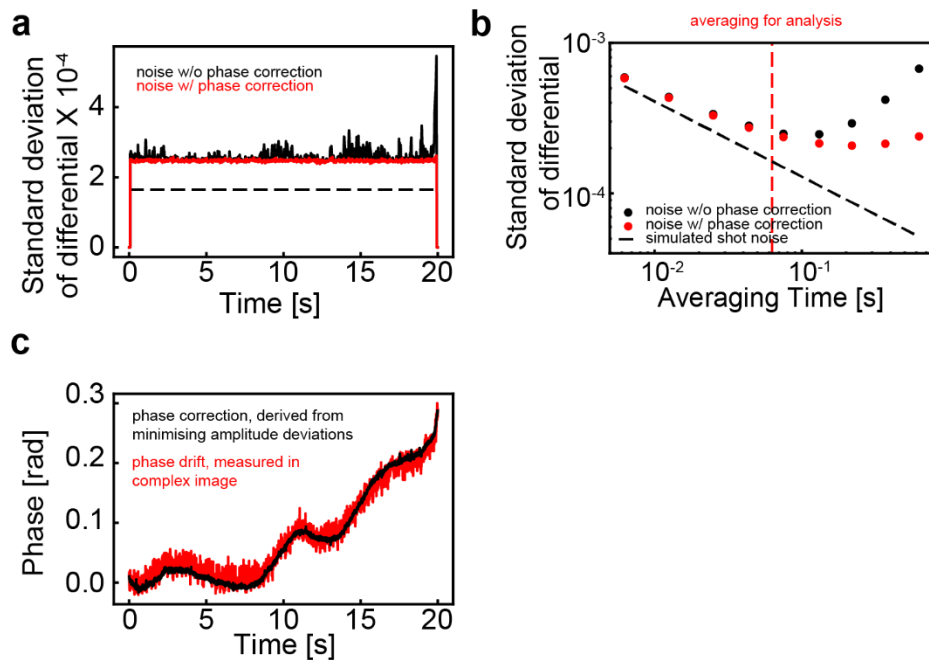
Supplementary Figure 8 – Precision of the PSF fit. A calculated complex PSF with random phase was placed in the centre (± 1 px) of a randomly selected thumbnail from a buffer measurement and a PSF fit was performed. For each mass, 2000 iterations with different thumbnails were performed. The resulting localisations were filtered in the same way as in the protein measurements. **a** Standard deviation of the difference between ground truth and fitted position in x and y. **b** Standard deviation of the fitted mass. **c** Standard deviation of the fitted phase and illumination corrected phase.



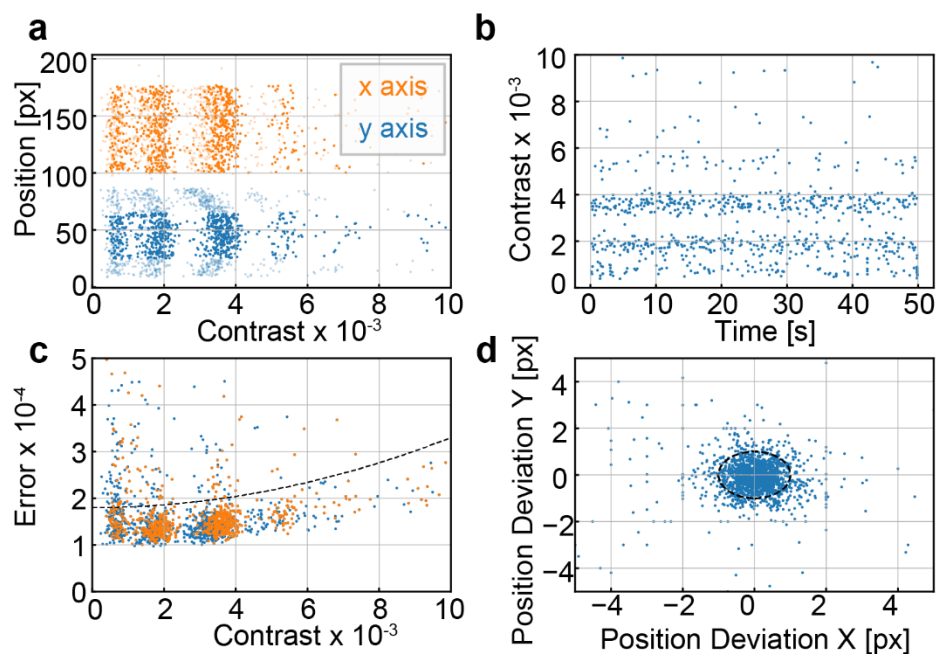
Supplementary Figure 9 – Single-protein contrast vs focusing during post-processing. a Histograms fitted with experimental PFSs for different focus positions. The red line corresponds to a sum of Gaussian distributions fitted to the histograms. **b** Real-part, imaginary-part, amplitude and phase of average point spread function model used to fit the data. **c** Resulting mass to contrast conversion values versus the standard deviation seen in the differential frames justifying the standard deviation as a good focus marker.



Supplementary Figure 10 – Photograph of the optical setup. The beam path of the illumination and reference are highlighted by a green line. The scattering path is indicated with a thick blue line.



Supplementary Figure 11 – Signal-to-noise. **a** Noise vs time of the differential of the complex valued scattered field for a movie containing no protein (buffer only). The red line indicates the noise trace after applying a phase correction on a frame-by-frame basis. **b** Standard deviation in the differential frames vs averaging time without phase correction (black data points) and with phase correction (red data points). The red dashed line indicates the averaging time used for the analysis of protein landing events. The black dashed line indicates the shot noise of a simulated movie with the same amount of detected photons per unit time compared to the experimental data. **c** Temporal phase evolution. The black curve is generated by minimising the amplitude differences to the first frame. The red trace indicates the phase measured in the complex raw data. The black trace is used to correct data in **a** and **b**.



Supplementary Figure 12 – Selection criteria for protein landing events. **a** Contrast vs x position (orange) and y position (blue) of each landing event. Only events in the centre along y axis (solid blue dots) are selected. **b** Temporal evolution of the selected events confirm axial stability during an acquisition. **c** Residuals of all fits. Events above a quadratic threshold (dashed black line) are neglected similar to Foley, et al.²⁵. **d** Deviation of fitted position from initial guess. Events which deviate more than 1 pixels from the initial guess (black dashed line) are discarded.